Theor Chem Acc (2004) 111:390–394
DOI 10.1007/s00214-003-0529-0

Theoretical
Chemistry Accounts

Regular article

Ab initio investigation of the vibrational hyper-Raman spectra of ethylene, ethane, and dimethyl ether

Olivier Quinet, Benoît Champagne

Laboratoire de Chimie Théorique Appliquée, Facultés Universitaires Notre-Dame de la Paix, rue de Bruxelles, 61, 5000 Namur, Belgium

Received: 14 February 2003 / Accepted: 30 April 2003 / Published online: 19 January 2004

Abstract. The time-dependent Hartree–Fock approach is employed with the aug-cc-pVDZ or 6-311++G** basis set to simulate, in the harmonic approximation, the hyper-Raman spectra of ethylene, ethane, and dimethyl ether. Comparison with the experiment of Verdieck et al. [(1970) *Chem. Phys. Lett.* 7:219] is performed for ethylene and ethane. Effects of the polarization of the incident light and the detected light are studied for ethylene. Special focus is given on these vibrational normal modes that cannot be detected in IR and Raman spectroscopies.

Keywords: Hyper-Raman spectroscopy – Time-dependent Hartree–Fock – Ethylene – Ethane – Dimethyl ether

Introduction

The hyper-Raman effect was first observed in 1965 by Terhune et al. [1]. It is a nonlinear inelastic scattering phenomenon where the exchange of energy between light and matter leads, typically, to rotational and vibrational transitions. Hyper-Raman spectroscopy provides complementary information to IR and Raman spectroscopies. In particular, hyper-Raman spectroscopy is helpful for studying low-frequency vibrational transitions which are difficult to detect with IR and Raman spectroscopies. Moreover, it may detect modes that are silent in both IR and Raman spectroscopies [2]. However, the hyper-Raman scattering cross-sections are small and, as a consequence, its utility is often limited and oriented towards resonance conditions [3] and/or surface-enhanced phenomena [4]. Several reviews on hyper-Raman spectroscopy [5, 6, 7] are available for interested readers.

Quantum chemical treatments of hyper-Raman spectroscopy are even rarer. All invoke the double harmonic oscillator approximation. To our knowledge, the first theoretical simulation was due to Golab et al. [4]. It tackles the orientation of pyridine adsorbed onto silver electrodes and it is based on the application of the π-electron Pariser–Parr–Pople (PPP) method to isolated molecules. Later, the theoretical treatment was improved either by adopting the semiempirical intermediate neglect of differential overlap (INDO) scheme or by performing ab initio Hartree–Fock calculations [8, 9]. Although the finite frequency of the incident beam was taken into account in the semiempirical (PPP and INDO) treatments, the Hartree–Fock simulations were based on normal coordinate derivatives of the static first hyperpolarizability, i.e. $(\partial\beta(0;0,0)/\partial Q_a)_0$, where Q_a is the ath vibrational normal coordinate and the subscript 0 means that the derivatives are taken at equilibrium geometry. However, it should be pointed out that in the PPP and INDO treatments the Q_a which are used to evaluate the $\partial\beta/\partial Q_a$ terms were obtained either from empirical force field [4, 8] or from the corresponding ab initio Hartree–Fock calculations [8]. Other semiempirical simulations of hyper-Raman spectra were carried out by Nørby Svendsen and Stroyer-Hansen by using a variational approach within the CNDO/2 approximation [10]. An extended basis set with polarization functions was used and the importance of taking into account the frequency of the incident light on the hyper-Raman intensities for methane, ethylene, and ethane was stressed. However, Ref. [10] does not provide clear evidence that theory can reproduce the features of the experimental hyper-Raman spectra. Although ab initio simulated hyper-Raman spectra are rare, the literature abounds in studies where the $\partial\beta(0;0,0)/\partial Q_a$ quantities are calculated. Indeed, together with $(\partial\mu/\partial Q_a)_0$, $(\partial\alpha(0;0)/\partial Q_a)_0$, and higher-order derivatives, these static quantities enter in the

Contribution to the Jacopo Tomasi Honorary Issue

Correspondence to: O. Quinet
e-mail: olivier.quinet@fundp.ac.be

evaluation of the vibrational polarizabilities and hyperpolarizabilities [11, 12].

Last year two analytical procedures based on the time-dependent Hartree–Fock (TDHF) scheme were elaborated to evaluate the first derivatives of the dynamic first hyperpolarizability with respect to atomic Cartesian coordinates and subsequently to simulate the nonresonant hyper-Raman spectra within the double harmonic approximation [13]. So far, this procedure has been applied to characterize the frequency-dispersion effects on the hyper-Raman intensities of three prototypical molecules, H_2O, NH_3, and CH_4. For instance, it was found that when going from $\hbar\omega = 0$ to $\hbar\omega = 1.165$ eV ($\lambda = 1{,}064$ nm) the hyper-Raman intensity can increase by more than 40% and that the frequency dispersion is not monotonic in all cases. Furthermore, it was demonstrated that, for "large intensity" modes, the aug-cc-pVDZ and Sadlej POL basis sets provide similar hyper-Raman intensities, whereas the intensities calculated with the 6-31++G** and cc-pVDZ basis sets are generally larger by a factor that can be as large as 2 [14].

These preliminary investigations are extended in this paper by simulating and analyzing the hyper-Raman spectra of three other molecules: ethylene, ethane, and dimethyl ether. Together with methane, the spectra of the first two molecules were recorded by Verdieck et al. [15], whereas dimethyl ether is one of those molecules possessing low-frequency IR-silent and Raman-silent vibrational modes.

This paper is dedicated to Jacopo Tomasi, who has been a pioneer in the theoretical treatment of solvent effects and in the development of polarizable continuum models for a large range of properties encompassing thermochemistry, electronic and vibrational spectroscopies, NMR, nonlinear optics, and many more. In spite of the limitation of the present paper to gas-phase molecules, there are many reasons to believe that its generalization to liquid and adsorbed phases will follow the procedures elaborated by him and coworkers for the Raman effect [16, 17, 18].

Methodology and computational procedure

For the Stokes band, the intensity of the scattered radiation associated with the ath vibrational normal mode of pulsation, ω_a, reads

$$\Im_{\mathrm{hR},a}(2\omega-\omega_a) \propto \mathrm{N}\Im_0^2(2\omega-\omega_a)^4 \times [1-\exp(-\hbar\omega_a/kT)]^{-1}\left|\left\langle \Psi_{\mathrm{init}}\middle|\hat{\beta}(\omega,Q)\middle|\Psi_{\mathrm{fin}}\right\rangle\right|^2 , \tag{1}$$

where ω is the angular frequency of the incident radiation, N is the number of molecules, $\Im_0$ is the intensity of the incident radiation, k is the Boltzmann constant, T is the temperature, and $\langle\Psi_{\mathrm{init}}|\hat{\beta}(\omega,Q)|\Psi_{\mathrm{fin}}\rangle$ is a matrix element of the first hyperpolarizability operator, $\hat{\beta}(\omega,Q)$, between the initial and final wavefunctions. This bracket is usually evaluated by invoking the clamped-nucleus [19] and the double harmonic oscillator approximations. In these conditions, the square bracket or transition integral turns out to be proportional to $(\partial\beta(-2\omega;\omega,\omega)/\partial Q_a)_0$ weighted by the inverse of the square-root of ω_a, while the vibrational transition corresponds to the change of the vibrational quantum number of the ath mode by one unit only.

To enable comparison with experiment, two aspects must still be considered: the geometry of the experimental setup and the fact that in gases and liquids the molecules are free to assume all orientations with respect to the observer with equal probability. In the usual setup, the incident light is plane-polarized and the observation is made in the direction perpendicular to both the electric field and its propagation direction. In such a case the hyper-Raman scattering intensity reads

$$\Im_{\mathrm{hR},a}(2\omega-\omega_a) \propto \mathrm{N}\hbar\Im_0^2\tfrac{(2\omega-\omega_a)^4}{2\omega_a}[1-\exp(-\hbar\omega_a/kT)]^{-1}I_{\mathrm{hR},a}(\omega) = N\hbar\Im_0^2\tfrac{(2\omega-\omega_a)^4}{2\omega_a}[1-\exp(-\hbar\omega_a/kT)]^{-1}\sum_{\varsigma,\eta}\left\langle\tilde{\beta}'^2_{\varsigma\eta\eta}(\omega,Q_a)\right\rangle, \tag{2}$$

where

$$\sum_{\zeta,\eta}\left\langle\tilde{\beta}'^2_{\zeta\eta\eta}(\omega,Q_a)\right\rangle = \left\langle\tilde{\beta}'^2_{\zeta\zeta\zeta}\right\rangle + \left\langle\tilde{\beta}'^2_{\zeta\eta\eta}\right\rangle, \tag{3}$$

with

$$\left\langle\tilde{\beta}'^2_{\zeta\zeta\zeta}\right\rangle = \tfrac{1}{7}\sum_{\zeta}^{x,y,z}\beta'^2_{\zeta\zeta\zeta} + \tfrac{4}{35}\sum_{\zeta\neq\eta}^{x,y,z}\beta'^2_{\zeta\zeta\eta} + \tfrac{2}{35}\sum_{\zeta\neq\eta}^{x,y,z}\beta'_{\zeta\zeta\zeta}\beta'_{\zeta\eta\eta} + \tfrac{4}{35}\sum_{\zeta\neq\eta}^{x,y,z}\beta'_{\eta\zeta\zeta}\beta'_{\zeta\zeta\eta} + \tfrac{4}{35}\sum_{\zeta\neq\eta}^{x,y,z}\beta'_{\zeta\zeta\zeta}\beta'_{\eta\eta\zeta} + \tfrac{1}{35}\sum_{\zeta\neq\eta}^{x,y,z}\beta'^2_{\eta\zeta\zeta} + \tfrac{4}{105}\sum_{\zeta\neq\eta\neq\xi}^{x,y,z}\beta'_{\zeta\zeta\eta}\beta'_{\eta\xi\xi} + \tfrac{1}{105}\sum_{\zeta\neq\eta\neq\xi}^{x,y,z}\beta'_{\eta\zeta\zeta}\beta'_{\eta\xi\xi} + \tfrac{4}{105}\sum_{\zeta\neq\eta\neq\xi}^{x,y,z}\beta'_{\zeta\zeta\eta}\beta'_{\xi\xi\eta} + \tfrac{2}{105}\sum_{\zeta\neq\eta\neq\xi}^{x,y,z}\beta'^2_{\zeta\eta\xi} + \tfrac{4}{105}\sum_{\zeta\neq\eta\neq\xi}^{x,y,z}\beta'_{\zeta\eta\xi}\beta'_{\eta\zeta\xi}, \tag{4}$$

$$\left\langle\tilde{\beta}'^2_{\zeta\eta\eta}\right\rangle = \tfrac{1}{35}\sum_{\zeta}^{x,y,z}\beta'^2_{\zeta\zeta\zeta} + \tfrac{4}{105}\sum_{\zeta\neq\eta}^{x,y,z}\beta'_{\zeta\zeta\zeta}\beta'_{\zeta\eta\eta} - \tfrac{2}{35}\sum_{\zeta\neq\eta}^{x,y,z}\beta'_{\zeta\zeta\zeta}\beta'_{\eta\eta\zeta} + \tfrac{8}{105}\sum_{\zeta\neq\eta}^{x,y,z}\beta'^2_{\zeta\zeta\eta} + \tfrac{3}{35}\sum_{\zeta\neq\eta}^{x,y,z}\beta'^2_{\zeta\eta\eta} - \tfrac{2}{35}\sum_{\zeta\neq\eta}^{x,y,z}\beta'_{\zeta\zeta\eta}\beta'_{\eta\zeta\zeta} + \tfrac{1}{35}\sum_{\zeta\neq\eta\neq\xi}^{x,y,z}\beta'_{\zeta\eta\eta}\beta'_{\zeta\xi\xi} - \tfrac{2}{105}\sum_{\zeta\neq\eta\neq\xi}^{x,y,z}\beta'_{\zeta\zeta\xi}\beta'_{\eta\eta\xi} - \tfrac{2}{105}\sum_{\zeta\neq\eta\neq\xi}^{x,y,z}\beta'_{\zeta\zeta\eta}\beta'_{\eta\xi\xi} + \tfrac{2}{35}\sum_{\zeta\neq\eta\neq\xi}^{x,y,z}\beta'^2_{\zeta\eta\xi} - \tfrac{2}{105}\sum_{\zeta\neq\eta\neq\xi}^{x,y,z}\beta'_{\zeta\eta\xi}\beta'_{\eta\zeta\xi}, \tag{5}$$

and

$$\beta'_{\zeta\eta\xi} = \left(\frac{\partial\beta_{\zeta\eta\xi}(-2\omega;\omega,\omega)}{\partial Q_a}\right)_0 . \tag{6}$$

For the anti-Stokes intensity, Eqs.(1) and (2) should be multiplied by the $\exp(-\hbar\omega_a/kT)$ factor and $(2\omega-\omega_a)$ replaced by $(2\omega+\omega_a)$. The $\langle\tilde{\beta}'^2_{\zeta\zeta\zeta}\rangle$ and $\langle\tilde{\beta}'^2_{\zeta\eta\eta}\rangle$ quantities, which are generally given in units of angstroms to the sixth power per atomic mass unit per statvolt squared, also define the depolarization ratio, i.e. the ratio between the scattered intensity which is perpendicularly polarized and the parallel-polarized intensity,

$$\rho_{\mathrm{hR},a}(\omega) = \frac{\left\langle\tilde{\beta}'^2_{\zeta\eta\eta}\right\rangle}{\left\langle\tilde{\beta}'^2_{\zeta\zeta\zeta}\right\rangle}. \tag{7}$$

The so-called depolarized lines are characterized by a depolarization ratio of 2/3 (e.g., the A_1 mode of methane), whereas it is smaller or larger for partly or completely polarized lines. An alternative setup where the incident radiation is circularly polarized and the scattered light is analyzed with polarization parallel to the scattering plane was also used in Ref. [15]. In this case and by employing the same approximations, the intensity of the scattered light reads [5, 20]

$$\Im_{\mathrm{hR},a}(2\omega-\omega_a) \propto \mathrm{N}\hbar\Im_0^2 \frac{(2\omega-\omega_a)^4}{2\omega_a} \times [1-\exp(-\hbar\omega_a/\mathrm{kT})]^{-1}\left\langle \tilde{\beta}'^2_{\zeta\eta\xi}(\omega,Q_a)\right\rangle \ , \quad (8)$$

with

$$\left\langle \tilde{\beta}'^2_{\zeta\eta\xi}\right\rangle = \tfrac{4}{105}\sum_{\zeta}^{x,y,z}\beta'^2_{\zeta\zeta\zeta} - \tfrac{4}{105}\sum_{\zeta\neq\eta}^{x,y,z}\beta'_{\zeta\zeta\zeta}\beta'_{\zeta\eta\eta} - \tfrac{8}{105}\sum_{\zeta\neq\eta}^{x,y,z}\beta'_{\zeta\zeta\zeta}\beta'_{\eta\eta\zeta} + \tfrac{4}{21}\sum_{\zeta\neq\eta}^{x,y,z}\beta'^2_{\zeta\zeta\eta} + \tfrac{4}{35}\sum_{\zeta\neq\eta}^{x,y,z}\beta'^2_{\zeta\eta\eta} - \tfrac{8}{105}\sum_{\zeta\neq\eta}^{x,y,z}\beta'_{\zeta\zeta\eta}\beta'_{\eta\zeta\zeta} - \tfrac{2}{21}\sum_{\zeta\neq\eta\neq\xi}^{x,y,z}\beta'_{\zeta\eta\eta}\beta'_{\zeta\xi\xi} - \tfrac{4}{35}\sum_{\zeta\neq\eta\neq\xi}^{x,y,z}\beta'_{\zeta\zeta\xi}\beta'_{\eta\eta\xi}, + \tfrac{16}{105}\sum_{\zeta\neq\eta\neq\xi}^{x,y,z}\beta'_{\zeta\zeta\eta}\beta'_{\eta\xi\xi} + \tfrac{22}{105}\sum_{\zeta\neq\eta\neq\xi}^{x,y,z}\beta'^2_{\zeta\eta\xi} - \tfrac{4}{35}\sum_{\zeta\neq\eta\neq\xi}^{x,y,z}\beta'_{\zeta\eta\xi}\beta'_{\eta\zeta\xi}.$$

In our simulations, the scattering peaks were described by Lorentzian functions with $\Gamma = 100$ wavenumbers (25 wavenumbers for dimethyl ether) and the vibrational frequencies were multiplied by the 0.91 factor to account for electron correlation and anharmonicity effects.

The $(\partial\beta(-2\omega;\omega,\omega)/\partial Q_a)_0$ quantities were evaluated analytically by adopting the TDHF scheme described in Refs. [13, 14] and implemented in GAMESS [21]. In order to reduce the computational task, the "less-iterative" scheme, invoking the $2n+1$ rule [22] and the interchange relations [23], was employed. The calculations were carried out with the aug-cc-pVDZ (ethylene and ethane) and 6311++G** (dimethyl ether) basis sets and for $\lambda = 694.3$ nm (corresponding to $\hbar\omega = 1.786$ eV) and $T = 298.15$ K. The vibrational normal modes have been labeled according to Ref. [24].

Results and discussion

The characteristics of the hyper-Raman spectra of ethylene are given in Table 1, while a comparison between the experimental spectrum of Verdieck et al. [15] and the TDHF/aug-cc-pVDZ simulation is provided in Fig. 1. The theoretical treatment confirms the fact that the broad peak at 3,040 wavenumbers [15] is an overlap between the ω_9 (B_{2u}) and ω_{11} (B_{3u}) C–H stretching bands; however, as shown in the simulated spectrum by the shoulder towards high frequencies, the relative hyper-Raman intensities of the cis (ω_9) and anti ω_{11} C–H stretching appear inverted in the simulation. This can, in principle, be attributed to the lack of electron correlation and anharmonicity effects; however, since this is beyond the scope of this paper, the relative importance of both effects is not addressed here. The ω_{12} (B_{3u}) mode associated with scissor motions is too weak and experimentally is not observed. The strong band at 980 wavenumbers is due to the ω_7 (B_{1u}) out-of-plane CH_2 wagging motion as well as, to a lower extent, to the ω_1 (A_u) twisting mode. The ω_{10} (B_{2u}) rocking mode predicted at 803 wavenumbers is not detected because the intensity is very small. In the simulation, the latter appears as a small shoulder on the left of the band around 1,000 wavenumbers. It should be noted that the ω_4 (A_u) twisting mode is silent in both IR and Raman (harmonic) spectroscopies and that, in this hyper-Raman experiment, it cannot be isolated owing to the proximity with the intense ω_7 (B_{1u}) bending mode. On the other hand, when simulating the spectrum using Eq. (8) (Fig. 2), the relative intensity of the ω_7 mode decreases with respect to the intensity of the ω_4 mode in such a way that the peak on the spectrum around 1,000 wavenumbers is mostly due to the ω_4 (A_u) twisting mode. These TDHF-based theoretical simulations constitute therefore a useful tool to analyze the hyper-Raman spectra for different experimental setups and, in particular, to assign unambiguously the band at 1,000 wavenumbers in Fig. 2 to the A_u vibration. Moreover, replacing the dynamic $(\partial\beta/\partial Q_a)_0$ quantities by their static analogues results for some vibrational normal modes in variations of the relative intensities that can be larger than 50%, confirming, therefore, the conclusions drawn in Ref. [10].

For ethane, theory reproduces the intense scattering peak at 2,950 wavenumbers which is attributed to the ω_5 (A_{2u}) and ω_7 (E_u) C–H stretching vibrations (Fig. 3, Table 2). As assumed in Ref. [15], the double peak near 1,450 wavenumbers comes from two vibrational normal modes, the umbrella-like ω_6 (A_{2u}) mode and the bending ω_8 (E_u) bending mode. Verdieck et al. [15]

Table 1. Scaled harmonic frequencies, ω_a (wavenumbers), relative hyper-Raman scattering intensities, $\Im_{\mathrm{hR},a}$ (%), and depolarization ratio of the hyper-Raman-active vibrational normal modes of ethylene calculated at the time-dependent Hartree–Fock (*TDHF*)/aug-cc-pVDZ level for $\lambda = 694.3$ nm

	ω_a	$\Im_{\mathrm{hR},a}$ (Eq. 2)	$\rho_{\mathrm{hR},a}$ (ω)	Exp. [15]	$\Im_{\mathrm{hR},a}$ (Eq. 8)
ω_{10} (B_{2u})	803	6	0.64		11
ω_7 (B_{1u})	984	100	0.16	980	28
ω_4 (A_u)	1,023	52	0.67		100
ω_{12} (B_{3u})	1,430	1	0.66	–	3
ω_{11} (B_{3u})	2,988	20	0.67	3,040	39
ω_9 (B_{2u})	3,087	11	0.54		16

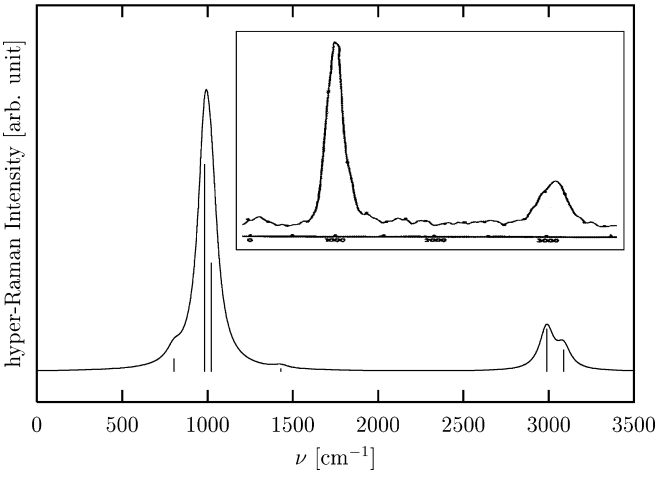

Fig. 1. Simulated hyper-Raman scattering spectrum for the Stokes band of ethylene based on the time-dependent Hartree–Fock (*TDHF*)/aug-cc-pVDZ results ($\lambda = 694.3$ nm, full width at half maximum (*FWHM*) = 100 cm^{-1}, $T = 298.15$ K) in comparison with the spectrum (*inset*) of Verdieck et al. [15] for the conventional experimental setup (plane-polarized incident light and detection of the total scattered light). (The experimental spectrum is reproduced from Ref. [15] copyright 1970 with permission from Elsevier Science)

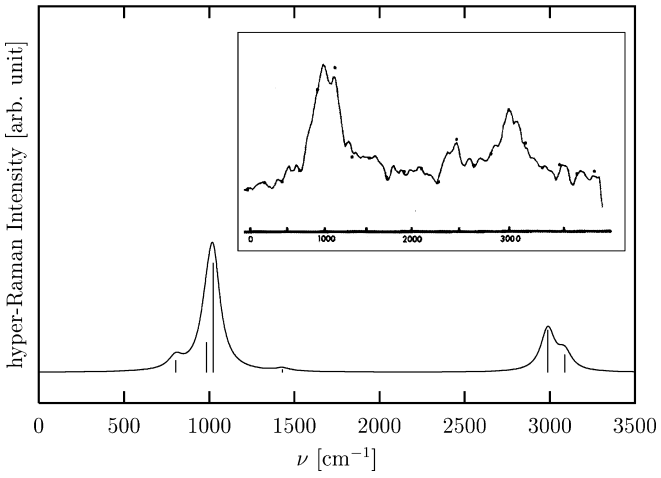

Fig. 2. Simulated hyper-Raman scattering spectrum for the Stokes band of ethylene based on the TDHF/aug-cc-pVDZ results ($\lambda = 694.3$ nm, FWHM = 100 cm^{-1}, $T = 298.15$ K) in comparison with the spectrum (*inset*) of Verdieck et al. [15] for a nonconventional experimental setup (circularly polarized incident light and detection of the scattered light polarized parallel to the scattering plane). (The experimental spectrum is reproduced from Ref. [15] copyright 1970 with permission from Elsevier Science)

attributed the band in the 900-wavenumber region to the ω_9 (E_u) bending mode. In better agreement with Table 105 of Ref. [24] the ω_9 bending mode frequency was estimated by the scaled restricted Hartree–Fock/aug-cc-pVDZ calculations to be 793 wavenumbers. It is highly probable that this 100-wavenumber difference is due to the weakness of the nonlinear scattering signal in Ref. [15]. The hyper-Raman simulation also confirms that the peak detected at 300 wavenumbers [15], and which is silent in both IR and Raman spectroscopies, is associated with the torsional mode of

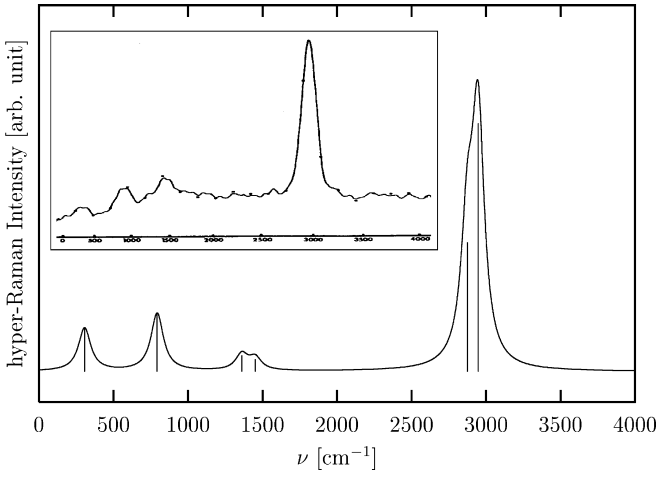

Fig. 3. Simulated hyper-Raman scattering spectrum for the Stokes band of ethane based on the TDHF/aug-cc-pVDZ results ($\lambda = 694.3$ nm, FWHM = 100 cm^{-1}, $T = 298.15$ K) in comparison with the spectrum (*inset*) of Verdieck et al. [15] for the conventional experimental setup (plane-polarized incident light and detection of the total scattered light). (The experimental spectrum is reproduced from Ref. [15] copyright 1970 with permission from Elsevier Science)

Table 2. Scaled harmonic frequencies, ω_a (wavenumbers), relative hyper-Raman scattering intensities, $\mathfrak{I}_{\mathrm{hR},a}$ (%), and depolarization ratio of the hyper-Raman-active vibrational normal modes of ethane (staggered conformation) calculated at the TDHF/aug-cc-pVDZ level for $\lambda = 694.3$ nm

	ω_a	$\mathfrak{I}_{\mathrm{hR},a}$ (Eq. 2)	$\rho_{\mathrm{hR},a}(\omega)$	Exp. [15]
ω_4 (A_{1u})	306	29	0.67	300
ω_9 (E_u)	793	24	0.53	900
ω_6 (A_{2u})	1,361	7	0.50	1,450
ω_8 (E_u)	1,451	5	0.67	
ω_5 (A_{2u})	2,875	52	0.29	2,950
ω_7 (E_u)	2,947	100	0.23	

A_{1u} symmetry. Therefore, like for ethylene, the TDHF-based simulation of the hyper-Raman spectrum of gas-phase ethane turns out to be in overall good agreement with experiment for both the vibrational frequencies and the intensities.

The comparison in Fig. 4 between the simulated IR, Raman, and hyper-Raman spectra of dimethyl ether shows that the aspect of the spectrum depends on the type of spectroscopy. The Raman spectra were simulated following the TDHF-based method described

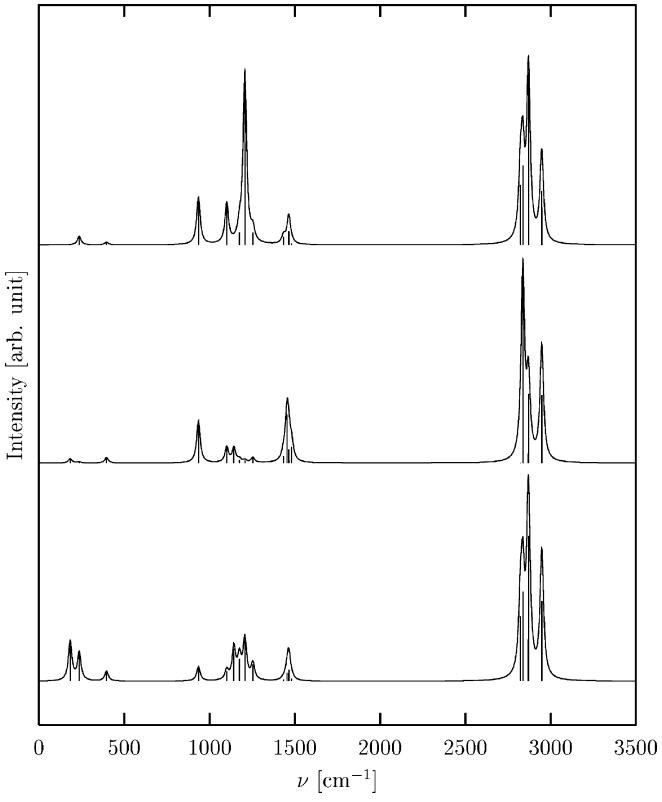

Fig. 4. Simulated IR (*top*), Raman ($\lambda = 532.0$ nm, $T = 298.15$ K, *middle*), and hyper-Raman ($\lambda = 694.3$ nm, $T = 298.15$K, *bottom*) spectra of dimethyl ether based on the TDHF/6-311++G** results (FWHM = 25 cm^{-1}). The conventional experimental setup (plane-polarized incident light and detection of the total scattered light) is assumed for Raman and hyper-Raman

in Ref. [25]. In the three cases, the bands associated with the CH stretching modes are intense. The Raman spectrum has a band at 1,455 wavenumbers which is associated with depolarized bending motions, whereas in the IR spectrum, there is a strong band at 1,207 wavenumbers due to the COC bending mode. Moreover, Fig. 4 shows that only hyper-Raman spectroscopy can detect the two low-frequency CH_3 twisting modes. Indeed, in the IR spectrum, the ω_{11} (A_2) symmetric mode is not active (in the harmonic approximation) and the ω_{21} (B_2) asymmetric mode has low intensity. In the Raman spectrum, the relative intensity is of the order of 1% or less and both modes are depolarized (for plane-polarized incident light, $\rho_{\mathrm{R},a}=3/4$). On the other hand, the relative intensities of these twisting modes are relatively large in the hyper-Raman spectrum, enabling their detection and their assignment. The ω_{11} (A_2) mode is, for the hyper-Raman spectrum, depolarized ($\rho_{\mathrm{hR},a}=2/3$), whereas the ω_{21} (B_2) mode is partly polarized ($\rho_{\mathrm{hR},a}=0.43$).

Conclusions

The hyper-Raman spectra of ethylene, ethane, and dimethyl ether have been simulated by using, within the clamped-nucleus and harmonic approximations, the recently-elaborated analytical TDHF approach with the aug-cc-pVDZ or 6-311++G** basis set. Comparison with experimental spectra for ethylene and ethane shows that this method reproduces most of the experimental features, including the variations of intensities associated with changing the polarization of the incident and detected light. Therefore, it supports the use of this approach to study these vibrational normal modes that are silent or almost silent in IR and Raman spectroscopies. This concerns here the twisting modes of ethylene, ethane, and dimethyl ether.

Acknowledgements. O.Q. and B.C. thank the Belgian National Fund for Scientific Research for their Postdoctoral Researcher and Senior Research Associate positions, respectively. The calculations were performed on a cluster of personal computers acquired thanks to a "crédit aux chercheurs" of the FNRS.

References

1. Terhune RW, Maker PD, Savage CM (1965) Phys Rev Lett 14:681
2. Cyvin SJ, Rauch JE, Decius JC (1965) J Chem Phys 43:4083
3. Long DA, Stanton L (1970) Proc R Soc Lond Ser A 318:441
4. Golab JT, Sprague JR, Carron KT, Schatz GC, Van Duyne RP (1988) J Chem Phys 88:7942
5. Altmann K, Strey G (1982) J Raman Spectrosc 12:1
6. Kielich S (1983) In: Wolf E (ed) Progress in optics, vol XX, North-Holland, Amsterdam, p 155
7. Ziegler LD (1990) J Raman Spectrosc 21:769
8. Yang WH, Schatz GC (1992) J Chem Phys 97:3831
9. Yang WH, Hulteen J, Schatz GC, Van Duyne RP (1996) J Chem Phys 104:4313
10. Nørby Svendsen E, Stroyer-Hansen T (1992) J Mol Struct 266:423
11. Kirtman B, Champagne B (1997) Int Rev Phys Chem 16:389
12. Bishop DM (1988) Adv Chem Phys 104:1
13. Quinet O, Champagne B (2002) J Chem Phys 117:2481 (2002); the depolarization ratios for plane-polarized and unpolarized light were inverted in Tables IV, V, and Vl
14. Quinet O (2002) Elaboration of quantum chemical procedures for determining mixed derivatives with respect to Cartesian coordinates and oscillating electric fields; application to vibrational spectroscopies and nonlinear optical proparties. Presses Universitaires de Namur, Namur
15. Verdieck JF, Peterson SH, Savage CM, Maker PD (1970) Chem Phys Lett 7:219
16. Cappelli C, Corni S, Tomasi J (2001) J Chem Phys 115:5531
17. Corni S, Tomasi J (2001) Chem Phys Lett 342:135
18. Corni S, Tomasi J (2002) J Chem Phys 116:1156
19. Bishop DM, Kirtman B, Champagne B (1997) J Chem Phys 107:5780
20. Bersohn R, Pao YH, Frisch HL (1996) J Chem Phys 45:3184
21. Schmidt MW, Baldridge KK, Boatz JA, Elbert ST, Gordon MS, Jansen JH, Koseki S, Matsunaga M, Nguyen KA, Su SJ, Windus TL, Dupuis M, Montgomery JA (1993) J Comput Chem 14:1347
22. (a) Silverman JL, van Leuven JL (1967) Phys Rev 162:1175; (b) Nee TS, Parr RJ, Bartlett RJ (1976) J Chem Phys 64:2216
23. (a) Dalgarno A, Stewart AL (1958) Proc R Soc Lond Ser A 242:245; (b) Hirschfelder JO, Byers Brown W, Epstein ST (1964) Adv Quantum Chem 1
24. Herzberg G (1945) Molecular spectra and molecular structure, II. Infrared and Raman spectra of polyatomic molecules. Van Nostrand Reinhold, New York
25. Quinet O, Champagne B (2001) J Chem Phys 115:6293